DOI: 10.1002/ente.201402152

# Investigation of Printing-Based Graded Bulk-Heterojunction Organic Solar Cells

Christian G. Bottenfield,[a] Fanan Wei,[a] Hui Joon Park,[b] L. Jay Guo,[c] and Guangyong Li*[a]

A 2-step method involving the evaporation of solvent through surface encapsulation and induced alignment (ESSENCIAL) has been used to create a compositionally graded active layer of interspersed acceptor and donor domains by printing-based technologies, which can be used to fabricate solar cells with higher performance than that from traditional bulk heterojunction fabrication methods. Herein, to clarify the fundamental mechanism of the performance improvement, a multi-scale simulation has been conducted to compare solar cells resulting from these two types of processing. The multi-scale simulation identified the underlying improvements of the ESSENCIAL morphology over traditional morphologies. Monte Carlo simulations obtained higher hole-mobility values and lower monomolecular recombination rates for the ESSENCIAL-fabricated cells that, in conjunction with the optical and electrical components, showed higher short-circuit currents, fill factors, and efficiencies, as indicated experimentally. The simulation offers the unique ability to model the varied active layer compositions and elucidate the underlying solar cell physics of complex morphologies.

## Introduction

Through the observation of the photovoltaic effect in an illuminated symmetrical structure of Ag–NaCl–anthracene in 1959, Kallmann and Pope et al. discovered the first organic solar cell (OSC), boasting a modest efficiency of only $2\times10^{-6}$. Although unable to explain its working principles, the researchers hypothesized that different charge-transfer mechanisms must exist at each electrode.[1] Today, great advances in materials, fabrication, characterization, simulation, and theory have contributed to record organic solar cell efficiencies exceeding 10%, though routine efficiencies are still below 5%.[2,3] The allure of organic solar cells lies in their mechanical flexibility and affordability, a result of the abundance, low prices, and solution-based processing methods of OSCs to replace conventional deposition methods requiring high temperatures or vacuum environments. A distinct advantage that OSCs have over conventional inorganics is their strong light-absorbing properties. Organic materials, useful for thin-film applications, have high absorption coefficients, allowing OSCs to use active layers of only a few hundred nanometers in thickness while still absorbing a large fraction of the solar spectrum.[4] Generally considered more environmentally friendly, OSCs offer a cheap and versatile option for a wide variety of low-energy needs, but they lack viability as a major power source due to the present low performance. Research efforts center on increasing the power conversion efficiency (PCE) to promote OSC marketability.

Recently, University of Michigan researchers developed a novel printing-based process using evaporation of solvent through surface encapsulation and induced alignment (termed ESSENCIAL) of polymer chains by applied pressure, which utilized a gas-permeable cover layer for solution casting, and the performance of the bulk-heterojunction (BHJ) blend was optimized with improved and uniform distribution in the vertical direction.[5] This process was further extended to a 2-step consecutive process for a bilayer-like OSCs in which the donor and acceptor layers were applied in separate steps by using the ESSENCIAL process (Figure 1).[6] The organization of the donor could be improved during the first ESSENCIAL process, and the second ESSENCIAL step helps to maximize the interdiffusion of the acceptor into the donor layer. Therefore, the acceptor molecules spontaneously formed continuous pathways during their diffusion into the donor phase, thereby approaching a quasi-bicontinuous phase between the donor and acceptor domains. Consequently, a graded blend of photovoltaic polymers has experimentally attained near 100% internal quantum efficiency at the 600 nm wavelength, and this led to

[a] C. G. Bottenfield, F. Wei, Dr. G. Li
Department of Electrical and Computer Engineering
University of Pittsburgh
3700 O'Hara St., Pittsburgh, PA 15213 (USA)
E-mail: gul6@pitt.edu

[b] Dr. H. J. Park
Division of Energy Systems Research
Ajou University
Suwon (South Korea)

[c] Dr. L. J. Guo
Department of Electrical and Computer Science
University of Michigan
Ann Arbor, MI (USA)

Part of a Special Issue on "Printed Energy Technologies". To view the complete issue, visit:
http://onlinelibrary.wiley.com/doi/10.1002/ente.v3.4/issuetoc

  

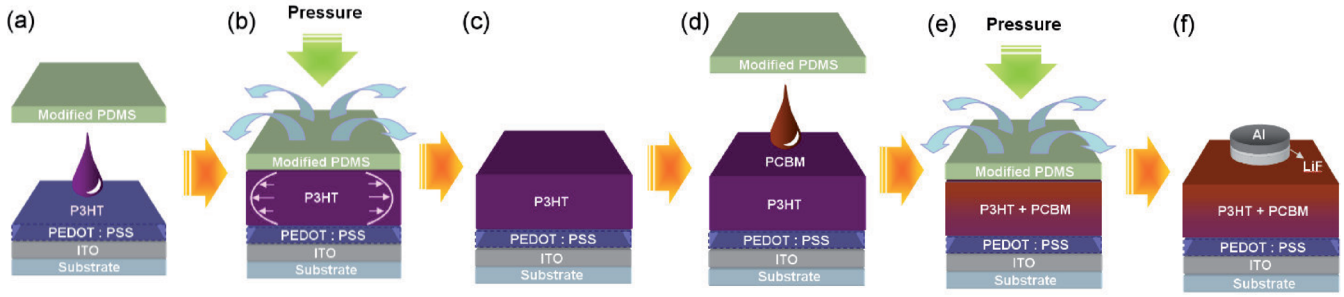


***Figure 1.*** Schematic of the 2-step ESSENCIAL process for the advanced heterojunction structure of polymer PV cell: a) Applying P3HT solution in chlorobenzene; b, c) P3HT layer formation during solvent evaporation under pressure; d) Applying the PCBM solution in dichloromethane; e) Active layer formation during solvent evaporation under pressure; f) Isolated island-type electrode deposition on top of the photoactive layer after removing the gas-permeable stamp. No post-annealing process (e.g., thermal treatment) is necessary. Reproduced with permission, Ref. [6], Copyright 2013, Wiley.

PCEs up to 4.71%, outperforming solar cells fabricated by other conventional methods. Further details on the ESSENCIAL method and characterization may be found elsewhere.[5,6] In this work, we focus on the graded heterojunction structures, based on the 2-step ESSENCIAL process (simply denoted as ESSENCIAL hereafter). Although the printing-based ESSENCIAL method has produced better results, it is not fully understood why the resulting solar cell morphology facilitates enhanced efficiencies. Simulations of the underlying device physics frequently serve as an accurate tool for studying the inner workings of complex solar cell devices. Properly identifying why this fabrication method's resulting morphology is superior will guide further research into developing solar cells to exhibit higher PCEs.

Organic solar cell simulations have found great success with a broad range of architectures, as quantified by their agreement with measurements and ability to identify interesting physics. Simulation packages, such as AMPS 1-D, although originally designed for inorganic solar cells, have been adapted to simulate organic solar cells, as performed by Babiker et al.[7] Other simulations, adopt a multi-faceted ground-up approach. One such work, performed by N. Li et al. takes advantage of optical and electrical simulations to study tandem organic solar cells and shows remarkable agreement with experimental values.[8] Another work by Gilot et al. simulates various tandem structures with the goal of optimization, a very powerful tool for researchers in guiding the design of solar cells.[9] Here again, optical and electrical components were used to more fully capture the complexity of the solar cell performance.

Our previous work has utilized a multi-faceted approach to achieve accurate device simulation through Monte Carlo, optical, and drift–diffusion model simulations.[10] The simulation in this work follows this strategy with significant modification to achieve the modeling of graded bulk-heterojunction OSCs as fabricated by the printing-based ESSENCIAL method. The modifications introduce multiple nanoscale layers into the optical simulation to vary the vertical composition of the active layer and mimic the ESSENCIAL morphology. Bulk effective medium approaches are maintained for each layer to reduce complexity and computation. Special care is taken to accurately determine the parameters of each layer's composition through advanced theory, as experimental studies on the properties of blended compositions are lacking. For the electrical simulation, Monte Carlo simulations provide information about the proper effective mobilities, recombination rates, and exciton dissociation efficiency (EDE) of the ESSENCIAL morphology. Together, the three components comprise a multi-scale simulation to explore the optics, morphology, and electrical characteristics of OSCs fabricated using the ESSENCIAL approach. This work identifies key improvements of the printing-based ESSENCIAL fabrication method over conventional methods.

## Results

In the BHJ solar cell, a continuous blend of donor (hole transporting) and acceptor (electron transporting) materials serves as the active layer to generate current from the photovoltaic effect, whereby excited states called excitons (coulombic-bound electron–hole pairs) are produced upon photon absorption by the active layer. Exciton formation occurs if the incident electromagnetic radiation has the minimum threshold frequency (i.e., energy) to promote an electron over the material's band gap from the highest occupied molecular orbital (HOMO) to the lowest unoccupied molecular orbital (LUMO). The energy of the incident radiation greater than the energy required to promote the electron is lost thermally. Thus, for efficient solar energy conversion, the band gap must match the photon energy as closely as possible. The strong coulombic interaction occurs in organic semiconductors but not in inorganic semiconductors due to the former's low dielectric constant and localized electron and hole wavefunctions.[11,12]

Excitons in organic semiconductors typically have binding energies of 0.1–1.4 eV, much higher than the few meV of inorganic counterparts.[9] Thus, the problem of separating excitons hindered OSC progress until Tang et al. introduced the heterojunction as an integral part of the organic solar cell.[13] The heterojunction allows for the efficient separation of excitons by providing a lower-potential configuration; that is, the electron and hole attain a more energetically favorable situation upon separation at the heterojunction.[14] Physically, the heterojunction creates a large interfacial area, allowing the

  

excitons generated within the exciton diffusion length to dissociate efficiently. Upon dissociation, carriers transport to their respective electrodes through drift and diffusion currents. The drift current is created by the carrier response to the electric field, primarily formed by the difference in work functions of the electrodes; the diffusion currents flow down the concentration gradients of each carrier. Electrons and holes are efficiently extracted by the electrodes if the donor HOMO and acceptor LUMO match the anode and cathode work functions, respectively.

The OSC simulation is composed of three component simulations: (1) the optical simulation, (2) the Monte Carlo simulation, and (3) the electrical device simulation. Together these components create a multi-scale tool, working from principles on the nanoscale morphology to those at the electrical device scale. A schematic of the multi-scale simulation is illustrated in Figure 2. The Monte Carlo simulation provides the macroscopic simulation with effective (bulk) mobilities, EDEs, and recombination coefficients. Through the optical simulation and the EDEs from the Monte Carlo simulation, the charge generation rate is acquired. Finally, the current–voltage curve ($J$–$V$), PCE, short-circuit current ($J_{SC}$), open-circuit voltage ($V_{OC}$), and fill factor ($FF$) are computed.

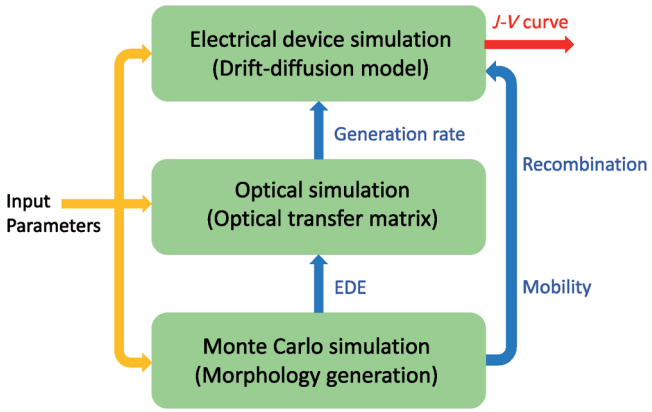


***Figure 2.*** Schematic of the multi-scale simulation.

### *Optical simulation*

Capturing the material properties' variation throughout the device is imperative to accurately simulating the graded bulk-heterojunction structure. Previous simulations, using effective material parameters for the bulk of the active layer, assumed no variation in the material parameters. The proposed simulation introduces multiple nanoscale layers to account for variation in the active layer and to investigate the enhanced processes leading to higher efficiencies of the ESSENCIAL morphology than the typical bulk-heterojunction morphology. The device architecture used in our simulation is shown in Figure 3.

The optical simulation determines the absorption rate, as a function of space (depth) and wavelength, in the active layer, which ultimately contributes to information about the generation rate of carriers and directly relates to the photocurrent. The simulation must take into account reflection and refraction, interference, absorption, and the intensity of the incident light. Here, we use the standard AM 1.5 solar spectrum data obtained from the National Renewable Energy Laboratory (NREL) for wavelengths in the range of 350–800 nm.[15] This range of wavelengths is justified because the glass strongly absorbs photons below 350 nm wavelengths, and P3HT:PCBM has too large of a bandgap for light with wavelengths greater than 800 nm.[16]

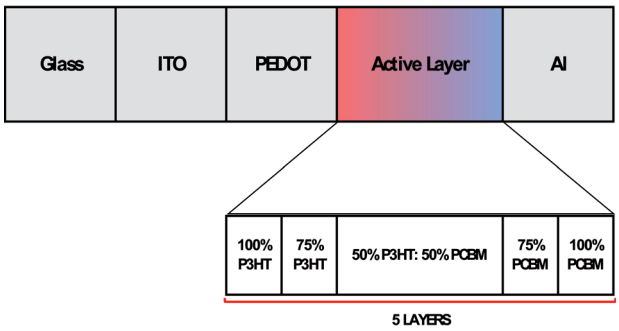


***Figure 3.*** Organic solar cell architecture and simplification of the active layer into discrete regions of varying P3HT:PCBM composition.

There are two main theories available upon which to base the optical simulation: (1) optical transfer matrix theory and (2) Beer–Lambert theory. Despite greater complexity, the absorption is calculated by the optical transfer matrix theory rather than the celebrated Beer–Lambert law due to the former's account for optical interference. In thin films, interference is introduced because the wavelengths are comparable in size to the thickness of the device.[16]

Complex values for the indices of refraction are necessary for both P3HT and PCBM materials to determine the indices of refraction of the intermediate layers of mixed composition. These data were obtained from the McGehee lab (Stanford University) transfer matrix data file.[17,18] Initially, the effective real and imaginary indices of refraction were calculated by a weighted average, but concern of oversimplification led to consideration of the Bruggeman effective medium theory, a mathematical method for calculating the resulting indices of refraction for a blend of two materials.[19] Numerically, the following must be solved for the permittivity of the mixed blend, $\varepsilon_M$:

$$f_A \frac{\varepsilon_A - \varepsilon_M}{\varepsilon_A + 2\varepsilon_M} + f_B \frac{\varepsilon_B - \varepsilon_M}{\varepsilon_B + 2\varepsilon_M} = 0 \quad (1)$$

in which $\varepsilon_A$ and $\varepsilon_B$ are the complex permittivities of materials A and B, and $f_A$ and $f_B$ are the volume fractions of materials A and B, respectively. The complex permittivities of the blended material are then expressed in the following form:

$$\varepsilon_M = \varepsilon_1 + i\varepsilon_2 \quad (2)$$

Then, the desired real and imaginary parts of the refractive indices are calculated using the following relations:

$$n = \sqrt{\frac{\sqrt{\varepsilon_1^2 + \varepsilon_2^2} + \varepsilon_1}{2}} \quad (3)$$

and

$$k = \sqrt{\frac{\sqrt{\varepsilon_1^2 + \varepsilon_2^2} - \varepsilon_1}{2}} \quad (4)$$

in which $n$ and $k$ represent the refractive (real) and absorptive (imaginary) coefficients of the complex refractive index, respectively. Figure 4 details the results of using the Bruggeman effective medium theory to estimate the complex refractive indices for various compositions. The results do not differ significantly and suggest that simple averaging methods are sufficient to obtain accurate optical coefficients for any composition of P3HT and PCBM.

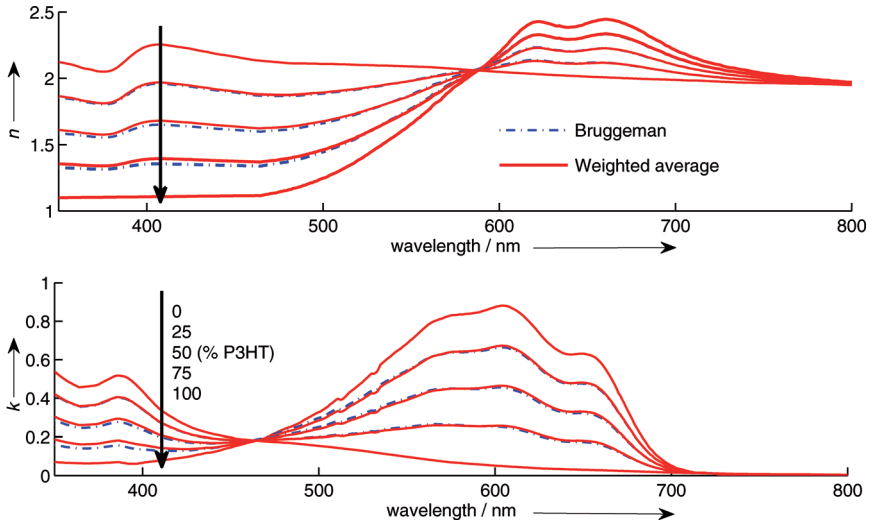


***Figure 4.*** Comparison of the Bruggeman effective-medium theory and the weighted average results for the complex indices of refraction of various P3HT:PCBM compositions, ranging from pure P3HT to pure PCBM.

With the proper optical coefficients for compositions of 100, 75, 50, 25, and 0% P3HT composition determined, each of the five layers were incorporated using the optical transfer matrix theory to mimic the ESSENCIAL approach's vertical variation. The results of the optical transfer matrix simulation match previous results reporting optimal (by optical consideration only) active layer thickness of approximately 90 and 240 nm.[16] Also, absorption in the device qualitatively resembles previous simulations, showing high absorption features at approximate depths of 120 and 300 nm.[6] However, our results, shown in Figure 5, indicate differences due to the discrete nature of the active layer structure. The absorption on the boundaries of the layers is discontinuous as it reflects the abrupt change in composition.

The simulation used an active layer thickness of 350 nm for the ESSENCIAL-fabricated solar cell to match the experimental dimensions. For the normal BHJ morphology, an active layer thickness of 320 nm was used, because this thickness displayed the best performance of the experimental cells and allows comparison of the ESSENCIAL morphology's performance to a strong representative of normal BHJ solar cells

Comparing the experimental data for the ESSENCIAL (layered) absorption to the normal BHJ (single-bulk) absorption yields seemingly counterintuitive results. Although the ESSENCIAL-fabricated cells displayed greater performance, the total absorption is actually lower for the ESSENCIAL simulation in comparison to the normal BHJ simulation. The normal BHJ structure absorbed a total of $3.32 \times 10^{21}$ photons $\times$ cm$^{-3}$, whereas the ESSENCIAL cell absorbed only $3.10 \times 10^{21}$ photons $\times$ cm$^{-3}$. The reduced absorption is due to the interfaces between layers of different compositions and increased destructive interference. These conclusions are clearly drawn from a close observation of the color maps provided in Figure 5. Although greater absorption occurs in the first 75 nm for the thicker BHJ cell (Figure 5c), the smaller 320 nm BHJ cell (Figure 5b) has greater absorption at depths beyond 75 nm. This phenomenon is the result of interference and allows the thinner BHJ cell to absorb more photons than its thicker counterpart. It is important to note that the bulk effective medium simulations cannot account for the reflective interfaces that occur in the BHJ structures. Although our layered approach certainly simplifies the complexity of the actual interfaces, it provides at least some account for such optical losses. A qualitative comparison of the absorption color maps for graded BHJ structures and normal BHJ structures is permitted upon study of Figure 5a and b. Specifically, noting the reduced absorption immediately following each interface in Figure 5a leads to the conclusion that the layer interfaces reflect light that is otherwise absorbed by the normal BHJ structure of Figure 5b. Thus, the internal reflective interfaces should be further investigated to assess their impact on absorption within both the ESSENCIAL and normal BHJ morphologies.

### *Monte Carlo simulation*

The Monte Carlo simulation is unique due to its ability to generate realistic morphologies that are utterly inexpressible in the electrical simulation and only partly accounted for by

  

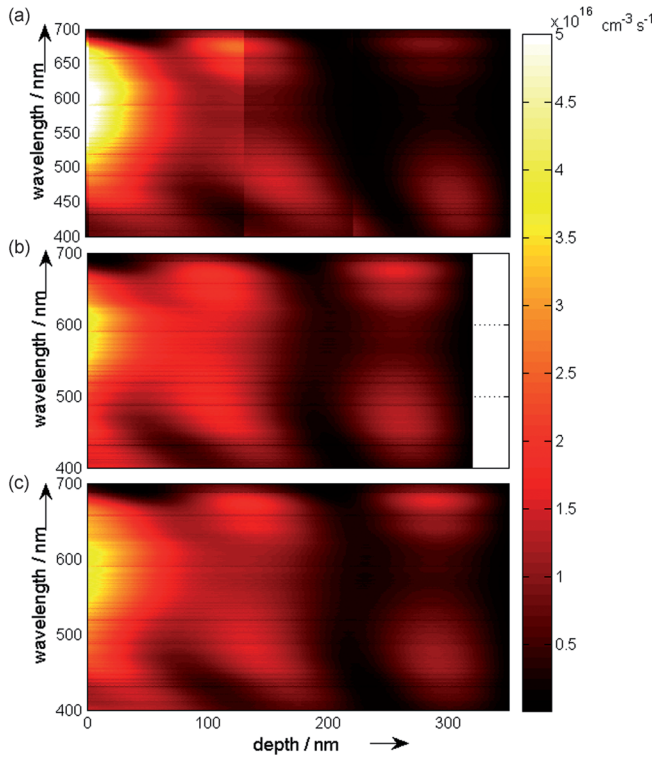


***Figure 5.*** Absorption color maps for a) 350 nm ESSENCIAL morphology, b) 320 nm normal BHJ morphology, and c) 350 normal BHJ morphology. Units are photons × $s^{-1}$ $cm^{-3}$.

the optical simulation. In this paper, the Monte Carlo simulation serves to calculate three important values: (1) the carrier mobilities, (2) the EDEs, and (3) the monomolecular recombination rates. The Monte Carlo simulation generated the normal BHJ and ESSENCIAL morphologies shown in Figure 5 d and e with connectivity and domain size data detailed in Table 1. The electron and hole mobilities were calculated

***Table 1.*** ESSENCIAL and BHJ domain sizes and connectivities.

| Type | Domain Size [nm] | Connected P3HT Ratio | Connected PCBM Ratio | Total Connectivity |
|---|---|---|---|---|
| BHJ | 22.1 | 0.993981 | 0.993891 | 0.993936 |
| ESS | 22.3 | 1.000000 | 0.989405 | 0.994733 |

as functions of the electric field, determined from the built-in voltage created by the difference in the electrode work functions and applied voltage.[20] Our experiment showed that bimolecular recombination was significantly suppressed in bilayer type devices by the ESSENCIAL printing method as compared with conventional BHJ structures.[6] Therefore, bimolecular recombination was ignored due to the apparent dominance of monomolecular recombination in the BHJ solar cells.[21]

To generate the ESSENCIAL morphology, the atomic force microscopy (AFM) phase image (Figure 6 a) is first transformed into a grayscale image. Using a histogram of grayscale values, the P3HT material is isolated by defining a threshold grayscale value of 71. The area of the P3HT material ($A_{P3HT}$) is quantified by a pixel count, and the edge length of P3HT ($l_{P3HT}$) is summed (Figure 6 b and c). As the AFM phase image indicates that the P3HT domains may assume ideal nanorod structures, the average diameter of the P3HT rods is approximately 21.9 nm according to the following estimation:

$$d = \frac{A_{P3HT}}{\frac{1}{2} l_{P3HT}} \tag{5}$$

In the ESSENCIAL method, the P3HT solution is dispensed onto a PEDOT:PSS layer and printed by using a gas-permeable silicon film. Subsequently, the PCBM solution is dispensed onto the P3HT layer and printed by the silicon film again. Under fair assumption, this process creates a gradient of P3HT and PCBM in the direction perpendicular to the device surface.

The ESSENCIAL morphology is generated by placing P3HT rods—simplified to average 20 nm in diameter—into a space with dimensions 180 nm × 180 nm × 350 nm. These P3HT rods are placed according to a vertical gradient distribution (Figure 6 f), and the P3HT length is assumed to obey a Gaussian distribution with an average length of 100 nm and standard deviation of 10 nm. To ensure that P3HT connectivity is sufficient, the volume-exclusion effect is ignored, that is, overlap between different P3HT rods is allowed. Mimicking the actual fabrication process, PCBM fills the remaining space in the morphology. The generated morphology is then discretized into small cubes with side lengths of 3 nm. To avoid the limited-volume effect, periodic boundary conditions are applied to the *x*- and *y*-axes, which are parallel to the device surface. The qualities of P3HT and PCBM connections are evaluated (along with the total connectivity) for the BHJ and ESSENCIAL morphologies. The total connectivities for the generated ESSENCIAL and BHJ morphologies are 0.9947 and 0.9939, respectively. The P3HT and PCBM connection ratios are shown in Table 1, along with the precise domain sizes of approximately 22 nm for each morphology. Further details on the normal BHJ morphology generation from the Ising model are provided elsewhere.[10]

Using the generated morphologies, Monte Carlo simulations calculate the effective mobilities, exciton dissociation efficiencies, and recombination rates. Further details on the Monte Carlo simulation are reported in our previous work.[7] The EDEs obtained from the Monte Carlo simulation are almost the same for both types of solar cells (78 %), however the carrier mobilities and recombination rates are very different. By varying the applied external voltage, the effective mobilities and recombination coefficients (shown in Figure 7 a and b >) are determined as functions of the net electric field in the device. For normal operation of both BHJ and ESSENCIAL solar cells, the electric field is usually less than $3 \times 10^4$ V $cm^{-1}$ in magnitude. At this range of electric fields, we can see that the hole mobility of ESSENCIAL

  

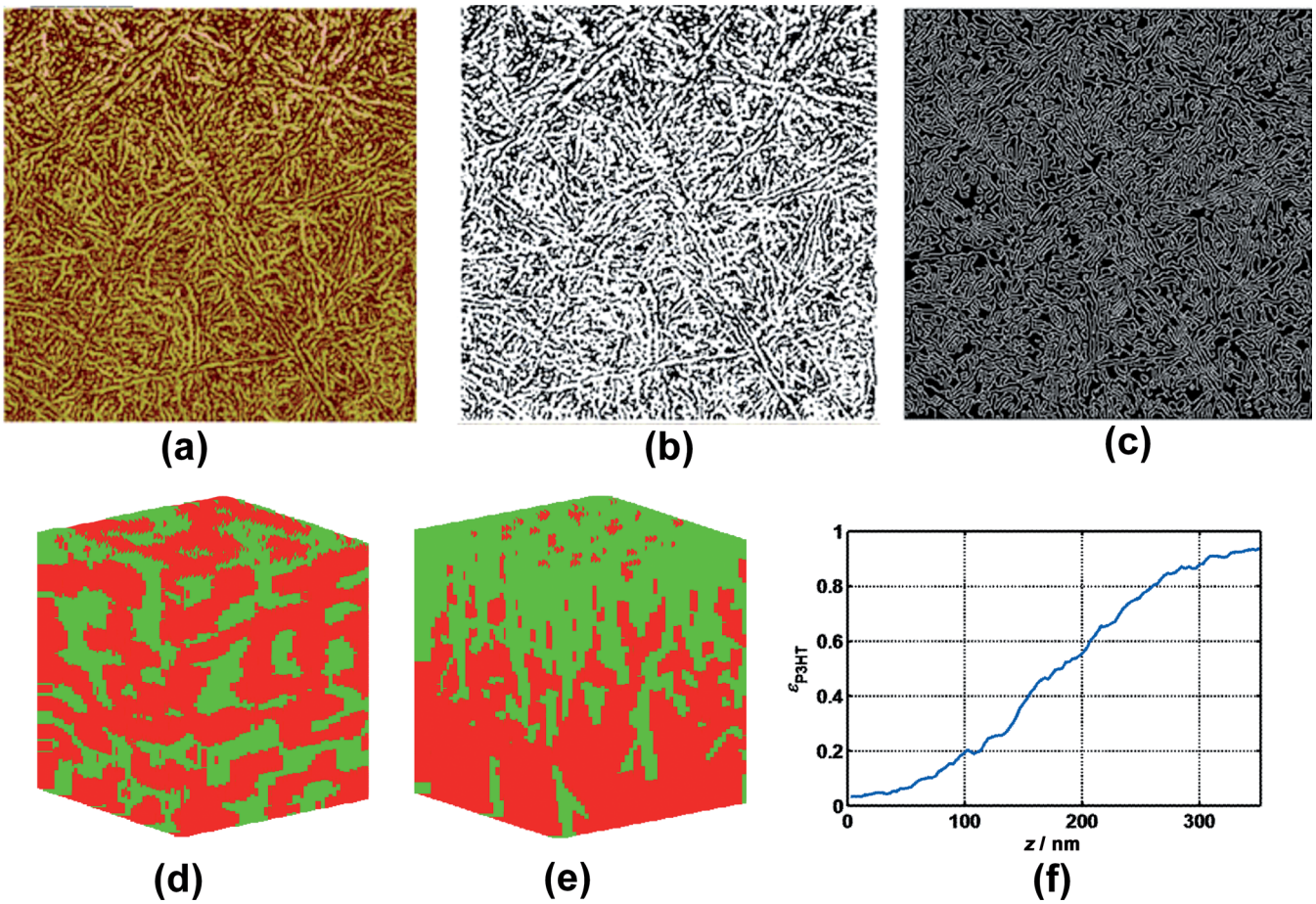


***Figure 6.*** a) AFM image of the experimental ESSENCIAL morphology, b) isolated P3HT after setting the threshold grayscale value, c) edge length of P3HT (white), d) generated normal BHJ morphology, e) generated ESSENCIAL morphology, and f) the vertical (*z*-direction) P3HT content of the ESSENCIAL morphology.

solar cells is significantly larger than that of the BHJ ones, whereas their electron mobilities are comparable, though the electron mobility of ESSENCIAL solar cells gradually decreases (Figure 7a). As we have known, the performance of OSCs is mainly limited by the hole mobility, typically one order of magnitude lower than its electron mobility. The enhancement of the hole mobility in ESSENCIAL solar cells is expected to improve the device performance. We can see that the monomolecular recombination in ESSENCIAL solar cells is also suppressed compared with that in BHJ ones. The suppressed recombination might be another reason for the enhanced performance of the ESSENCIAL solar cells. To further verify the performance enhancement; electrical simulation based on the parameters obtained from Monte Carlo simulation was performed for comparison between experiments and simulations. The trajectories of all excitons, electrons, and holes were recorded and used to determine the macroscale parameters.

### *Electrical simulation*

The previous component simulations provide the recombination rates, mobilities, EDEs, and absorption rates as inputs to the final electrical simulation, which calculates the *J*–*V* curve, *FF*, $J_{SC}$, $V_{OC}$, and efficiency.

The electrical simulation uses the drift–diffusion model, involving three governing equations: the Poisson equation and the two coupled continuity equations. The Poisson equation, relating the electric potential and charge (i.e., carrier density), is given by:

$$\frac{\partial^2}{\partial x^2}\varphi(x) = \frac{q}{\varepsilon}[n(x) - p(x)] \tag{6}$$

in which $\phi$ represents the electric potential, $q$ is the fundamental charge, $\varepsilon$ is the dielectric constant, and $n$ and $p$ are the electron and hole densities, respectively. The electron and hole continuity equations are respectively given by:

$$-n(x)\mu_n\frac{\partial^2\varphi}{\partial x^2} - \frac{\partial n}{\partial x}\mu_n\frac{\partial\varphi}{\partial x} + D_n\frac{\partial^2 n}{\partial x^2} = -G + R_n \tag{7}$$

and

$$-p(x)\mu_p\frac{\partial^2\varphi}{\partial x^2} - \frac{\partial p}{\partial x}\mu_p\frac{\partial\varphi}{\partial x} - D_p\frac{\partial^2 p}{\partial x^2} = G - R_p \tag{8}$$

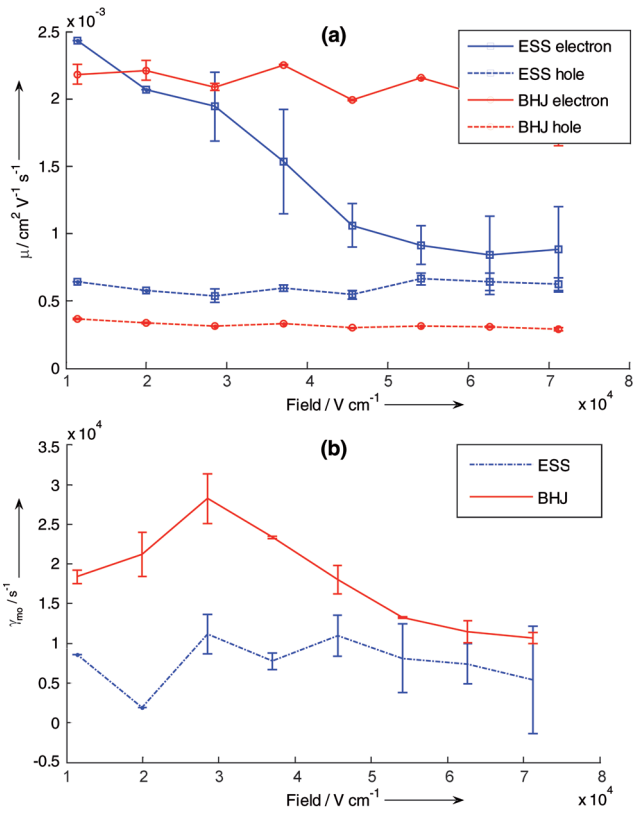


***Figure 7.*** a) Calculated mobilities for the ESSENCIAL and BHJ morphologies through Monte Carlo simulation, b) the monomolecular recombination coefficients calculated by Monte Carlo simulation.

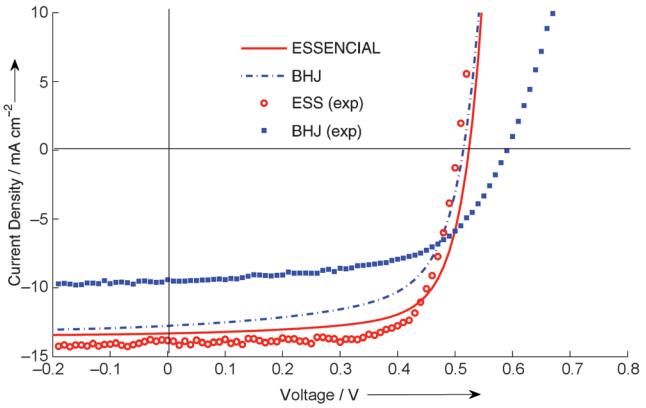


***Figure 8.*** Comparison of simulated and experimental *J–V* curves for the ESSENCIAL and normal BHJ morphologies.

***Table 2.*** Comparison of experimental and simulated performances for the ESSENCIAL and BHJ morphologies.

| Type | $J_{SC}$ [mA cm$^{-2}$] | $V_{OC}$ [V] | *FF* | PCE [%] |
|---|---|---|---|---|
| BHJ (experiment) | 9.38 ± 0.44 | 0.59 ± 0.00 | 58.96 ± 01.20 | 3.27 ± 0.17 |
| BHJ (simulation) | 12.77 | 0.51 | 62.70 | 4.12 |
| ESS (experiment) | 13.83 ± 0.52 | 0.51 ± 0.01 | 66.98 ± 5.05 | 4.71 ± 0.36 |
| ESS (simulation) | 13.33 | 0.52 | 69.57 | 4.86 |

in which $D_n(D_p)$ is the Einstein electron (hole) diffusion coefficient, $\mu_n(\mu_p)$ is the electron (hole) mobility, $R_n(R_p)$ is the electron (hole) recombination rate, and $G$ is the generation rate. To successfully solve these three equations simultaneously, numerical iteration is necessary, which requires the equations to be normalized, discretized, and linearized to make computation feasible. Details on the normalization, discretization, and linearization of the Poisson and continuity equations are explained elsewhere along with the decoupled iteration method.[16]

With the full drift–diffusion simulation developed, the *J–V* curves, PCE, $V_{OC}$, $J_{SC}$, and *FF* may be calculated. The resulting *J–V* curves for the ESSENCIAL and normal BHJ morphologies are shown in Figure 8, with the simulated data and the experimental data from previous work displayed in Table 2 for comparison. In our experimental results (Ref. [6]) the $J_{SC}$ values obtained by *J--V* curves for all PV cells were well matched to those calculated by EQE signals, with differences within 5%.[6] Although the simulation shows some deviation from the experimental data, both the simulated and experimental data showed higher $J_{SC}$, *FF*, and PCE values than their normal BHJ counterparts. Noticeable similarity between the simulated and experimental results for the ESSENCIAL morphology suggest the accuracy of the simulation. However, regarding $J_{SC}$ and $V_{OC}$, the simulated normal BHJ performance significantly strays from the experimental values and requires explanation. Also, close observation of the data reveals that the simulated $V_{OC}$ did not show the same trend as the experiments upon comparing the ESSENCIAL and normal BHJ morphologies. The experiments showed larger $V_{OC}$ for the normal BHJ morphology, whereas the simulations indicated the opposite conclusion. Nonetheless, the simulation results concur with experiments in recognizing the higher performance of the ESSENCIAL morphology. Particularly, the high fill factors for the simulated and experimental ESSENCIAL solar cells verify the suppression of monomolecular recombination in the ESSENCIAL morphology determined by using the Monte Carlo simulation.

To explain the increased $J_{SC}$ value of the ESSENCIAL morphology, one may give the most obvious answer that it is due to increased absorption by the active layer, as absorption directly contributes to the generation rate and thus the photocurrent. However, the results of the optical and Monte Carlo simulation are counterintuitive and inconsistent with such an explanation. Instead, we observe slightly higher absorption (≈7% more) in the normal BHJ solar cell than in the ESSENCIAL solar cell due to interference effects. Thus, by considering absorption only, one might erroneously conclude that the normal BHJ solar cell has better performance.

The true insights into the superiority of the ESSENCIAL approach are found in the Monte Carlo simulation. Perhaps this is not surprising because it generates the true morphology for the larger multi-scale simulation. From the Monte Carlo simulation we observed increased hole mobility,

a strong contributor to the increased $J_{SC}$. Also, the ESSENCIAL approach decreased monomolecular recombination in the device, thereby improving $J_{SC}$. Thus, the increased $J_{SC}$ of the ESSENCIAL morphology is accounted for.

## Discussion

To explain the deviation of the normal BHJ $J_{SC}$ from its experimental value, the Monte Carlo simulation is examined critically. The P3HT and PCBM connectivities (Table 1) determined during the Monte Carlo generation of the normal BHJ morphology are notably exceptional and do not represent the actual BHJ morphologies. These ideal connectivities result from the optimized morphology of the simulated BHJ structure. Such ideal connectivities result in increased carrier mobility and $J_{SC}$, which explains the higher $J_{SC}$ obtained in simulation than experiment for the normal BHJ morphology. This argument does not apply as strongly to the ESSENCIAL morphology, because the ESSENCIAL fabrication process facilitates greater connectivities. However, the ESSENCIAL simulated curve slightly deviated from the experimental curve, likely the result of only knowing the surface morphology from the AFM phase image but little about the internal morphology. Worthy of comment, the slightly higher EDE of the normal BHJ morphology is likely due to the greater intermixing of the donor and acceptor materials, as is noticeable from the generated morphologies. However, the high connectivities generated for the BHJ structure surely contribute to the EDE; thus, the calculated EDEs for the BHJ are likely higher than in the actual morphologies.

Regarding $V_{OC}$, our simulation actually showed a reversed trend to the experimental behavior. In the experiments $V_{OC}$ decreased with the ESSENCIAL approach, whereas the $V_{OC}$ slightly increased in our simulation. This contradiction remains to be solved.

It can be observed from the $J$–$V$ curves that the performance enhancement in ESSENCIAL solar cells is mostly attributed to the increased fill factor, changing from 63% (BHJ) to 70% (ESSENCIAL). Such a significant increase, observed both experimentally and by simulation, is mainly due to the suppressed recombination and enhanced hole mobility as revealed from the Monte Carlo simulations.

## Conclusions

Overall, in this work we have created a multi-scale simulation that captures the vertical variation of the active-layer composition. The model has suggested that the primary sources of the printing-based ESSENCIAL morphology's improvements over typical BHJ morphologies are increased hole mobility and decreased monomolecular recombination. Along the way, this simulation explored the optics, mobilities, recombination rates, and morphologies of the ESSENCIAL-fabricated solar cell and compared these results to the typical BHJ solar cell. Regarding a mixed P3HT:PCBM composite, a simple weighted average is sufficient to obtain the complex indices of refraction. Also, interference effects were observed to significantly affect absorption due to the similarity in the active layer thickness and incident wavelengths. Understanding the improvements of the printing-based ESSENCIAL fabrication method leads to a deeper understanding of the morphology's important role in solar cell performance.

## Experimental Section

The optical simulation was performed using the optical transfer matrix theory, in which each interface and layer are represented by a matrix. This theory is beyond the scope of this paper and is detailed in literature elsewhere.[13] The McGehee lab of Stanford University offers a free optical transfer matrix file that is suitable to perform the optical calculations here as well; however we did not take advantage of this and developed our own simulation. The index of refraction data for pure P3HT and pure PCBM were obtained from the McGehee lab's data file for wavelengths in the range of 300–800 nm, however.[15] Only wavelengths in the range of 300–800 nm were considered due to the constraints imposed by the active layer's effective band gap and the absorption of the glass. The Bruggeman effective medium theory was used to calculate the effective indices of refraction for mixed compositions of P3HT:PCBM; this involved solving a set of equations through iteration.[16] AM 1.5 solar spectrum data were obtained from the National Renewable Energy Laboratory.[12]

The ESSENCIAL Monte Carlo simulation was performed by first converting actual AFM phase images of the P3HT:PCBM surface into a computer-generated model composed of 3 nm blocks of P3HT and PCBM. Nanorods of P3HT were measured from the phase image and implemented into the model first according to a gradient distribution shown in Figure 6 f. The nanorods, averaging approximately 21.9 nm in diameter, filled a space of dimensions $180\,nm \times 180\,nm \times 350\,nm$; the volume-exclusion effect was ignored for simplification and periodic boundary conditions were applied to the $x$- and $y$-axes. The PCBM filled the remaining volume. The lengths of the P3HT rods was assumed to obey a Gaussian distribution with an average length of 100 nm and standard deviation of 10 nm. Details on the normal BHJ morphology generation can be found in other literature.[7]

The electrical simulation used the drift–diffusion model, performed by solving the Poisson equation, the electron continuity equation, and the hole continuity equation simultaneously through iteration. A decoupled iteration was used, the full details of which are identical to those in a previous work.[13] The mobilities, recombination rates, and generation rates in the electrical simulation were obtained from the optical and Monte Carlo simulations. Other parameters of the electrical simulation included an effective density of states of $N_C = 2 \times 10^{20}\,cm^{-3}$, a dielectric constant of $3.01 \times 10^{-13}\,F\,cm^{-1}$, an effective band gap of 1.05 eV, and a temperature of $T = 300$ K.

## Symbols

| | |
|---|---|
| BHJ | bulk heterojunction |
| $D_n(D_p)$ [$cm^2\,s^{-1}$] | electron (hole) diffusion coefficient |
| EDE [%] | exciton dissociation efficiency |
| ESSENCIAL/ESS | evaporation of solvent through surface encapsulation and induced alignment of polymer chains by applied pressure |
| $\varepsilon$ | dielectric constant or relative permittivity |

| | |
|---|---|
| $\varepsilon_M$ | effective dielectric constant of mixed materials |
| $f_A$ ($f_B$) | volume fraction of material A (B) |
| *FF* | fraction of power produced out of the total possible determined by the $V_{OC}$ and $J_{SC}$ |
| $G$ [excitons $\times$cm$^{-3}$s$^{-1}$] | exciton generation rate |
| HOMO (LUMO) [eV] | highest (lowest) occupied molecular orbital |
| $J_{SC}$ [mA cm$^{-2}$] | short-circuit current density |
| $k$ | imaginary part of index of refraction |
| $\mu_n(\mu_p)$ [cm$^2$V$^{-1}$s$^{-1}$] | electron (hole) mobility |
| $n$ | real part of index of refraction |
| $n(x)$ [cm$^{-3}$] | electron concentration |
| $p(x)$ [cm$^{-3}$] | hole concentration |
| OSC | organic solar cell |
| PCBM | [6,6]-phenyl-C 61-butyric acid methyl-ester, the acceptor material |
| PCE [%] | power conversion efficiency |
| PV | photovoltaic |
| P3HT | poly(3-hexylthiophene), the donor material |
| $\phi$ [V] | electric potential |
| $q$ [$1.602\times10^{-19}$] | electric charge |
| $R$ [cm$^{-3}$s$^{-1}$] | recombination rate |
| $V_{OC}$ [V] | open-circuit voltage |

## Acknowledgements

*This research is supported in part by the NSF grants CBET 1132819 and CBET 1404591, the Office of the Provost of the University of Pittsburgh, the Brackenridge Undergraduate Research Fellowship Program performed by University Honors College of the University of Pittsburgh, and the Swanson School of Engineering. H.J.P. and L.J.G. acknowledge partial support by the Center for Solar and Thermal Energy Conversion, an Energy Frontier Research Center funded by the U.S. Department of Energy, Office of Science, Basic Energy Sciences under Award DESC0000957.*

**Keywords:** composition grading · multi-scale simulation · nanotechnology · organic solar cells · printing

[1] H. Kallmann, M. Pope, *J. Chem. Phys.* **1959**, *30*, 585–586.
[2] M. A. Green, K. Emery, Y. Hishikawa, W. Warta, E. D. Dunlop, *Prog. Photovoltaics* **2012**, *20*, 12–20.
[3] NREL—National Renewable Energy Laboratory, *Best Research-Cell Efficiencies*, **2014**, http://www.nrel.gov/ncpv/.
[4] W. Brütting, *Physics of Organic Semiconductors*, Wiley, Weinheim, **2006**, 1–14.
[5] H. J. Park, M. G. Kang, S. H. Ahn, L. J. Guo, *Adv. Mater.* **2010**, *22*, E247–E253.
[6] H. J. Park, J. Y. Lee, T. Lee, L. J. Guo, *Adv. Energy Mater.* **2013**, *3*, 1135–1142.
[7] S. G. Babiker, Y. Shuai, *Res. J. Appl. Sci., Eng. Technol.* **2012**, *4*, 495–499.
[8] N. Li, D. Baran, K. Forberich, M. Turbiez, T. Ameri, F. C. Krebs, C. J. Brabec, *Adv. Energy Mater.* **2013**, *3*, 1597–1605.
[9] J. Gilot, M. M. Wienk, R. A. Janssen, *Adv. Mater.* **2010**, *22*, E67–E71.
[10] F. Wei, L. Liu, L. Liu, G. Li, *IEEE J. Photovoltaics* **2013**, *3*, 300–309.
[11] B. A. Gregg, M. C. Hanna, *J. Appl. Phys.* **2003**, *93*, 3605.
[12] A. Mayer, S. Scully, B. Hardin, M. Rowell, M. McGehee, *Mater. Today* **2007**, *10*, 28–33.
[13] C. W. Tang, *Appl. Phys. Lett.* **1986**, *48*, 183.
[14] C. J. Brabec, G. Zerza, G. Cerullo, S. De Silvestri, S. Luzzati, J. C. Hummelen, S. Sariciftci, *Chem. Phys. Lett.* **2001**, *340*, 232–236.
[15] NREL—National Renewable Energy Laboratory, *Reference Solar Spectral Irradiance: Air Mass 1.5*, *2013*, *AM 1.5 Spectrum Data*, http://rredc.nrel.gov/solar/spectra/am1.5/.
[16] L. Liu, PhD dissertation, University of Pittsburgh, **2011**, 152.
[17] G. F. Burkhard, E. T. Hoke, M. D. McGehee, *Adv. Mater.* **2010**, *22*, 3293–3297.
[18] M. McGehee, G. Burkhard, E. Hoke, *Transfer Matrix Optical Modeling*, **2014**, http://web.stanford.edu/group/mcgehee/.
[19] D. A. G. Bruggeman, *Ann. Phys.* **1935**, *416*, 636–664.
[20] R. Häusermann, E. Knapp, M. Moos, N. A. Reinke, T. Flatz, B. Ruhstaller, *J. Appl. Phys.* **2009**, *106*, 104507.
[21] L. Liu, G. Li, *Solar Energy Mater Solar Cells* **2011**, *95*, 2557–2563.

Received: October 15, 2014
Revised: November 22, 2014
Published online on March 12, 2015

  